Nanoscale

PAPER

View Article Online
View Journal | View Issue

Cite this: *Nanoscale*, 2024, **16**, 4858

Tunable 2-D magnonic crystals: effect of packing density

C. Tian[a] and A. O. Adeyeye *[a,b]

Magnonic crystals, periodic arrays of magnetic structures, have emerged as a promising platform for manipulating and controlling spin waves in magnetic materials. Magnetic antidot nanostructures, representing 2-D magnonic crystals, are versatile platforms for controlling and manipulating magnons. In this work, we systematically investigate the effects of inter-hole spacing and lattice (rhombic and honeycomb) arrangements on the dynamic properties of $Ni_{80}Fe_{20}$ antidot structures. The dynamic responses of antidot lattices of fixed hole diameter (d = 280 nm) and inter-hole spacing (s) between 90 and 345 nm are investigated using broadband ferromagnetic spectroscopy. Multiple resonance modes sensitive to s are observed due to the inhomogeneous internal field distribution induced by the presence of holes. There is a marked variation in mode frequency, mode intensity and the number of modes for rhombic antidot lattice as the inter-hole spacing and applied field direction are varied. Our experimental results are in good agreement with micromagnetic simulations. Our findings may find application in the design of magnonic-based devices.

Received 3rd November 2023,
Accepted 26th January 2024

DOI: 10.1039/d3nr05582e

rsc.li/nanoscale

Introduction

Magnonic crystals (MCs) are periodic arrays of magnetic structures that exhibit unique magnonic properties, including band gaps and tailored spin wave dispersion relations.[1–3] These periodic magnetic structures have garnered considerable attention due to their ability to control and manipulate spin waves or magnons.[4] In this context, magnetic antidot nanostructures, representing 2-D MCs, are versatile platforms for controlling and manipulating magnons.[5] The Spin wave (SW) modes and the magnonic band structure of antidot lattice can be tailored by varying the lattice symmetry,[6] lattice constant,[7] size and shape of the holes,[8,9] and orientation of the magnetic field.[10–15] The SW modes in antidot lattices exhibit a significant anisotropy induced by the lattice symmetry of the holes.[16] Field orientation and strength can control standing and propagating SWs in a square antidot lattice.[17] Significant effects of geometrical parameters of the square antidot lattice on SW modes and the formation of magnonic minibands have been observed.[7,10,18,19]

The magnetic properties of antidot structures with square lattice are extensively studied by varying the applied field orientation and strength,[17] hole diameter,[10] inter-hole spacing,[7] thickness,[19] and hole shape.[20] There are fewer reports in the literature on the experimental investigation of the effects of geometrical parameters on the magnetic properties of rhombic and honeycomb antidot lattices.[12]

In this study, we systematically investigated the dynamic behaviors displayed by rhombic and honeycomb Ni80Fe20 (permalloy, Py) antidots characterized by a fixed diameter (d = 280 nm) and varying inter-hole spacing (s) within the range of 90 nm to 345 nm. We observed that the FMR responses of antidot structures are highly sensitive to the s and H_{app} directions. Antidot lattices exhibit a significant tunability of the number of observed modes and mode frequency, which can be tailored by varying s and H_{app} directions.

Experimental details

Sample fabrication

Periodic arrays of circular holes arranged in rhombic and honeycomb lattices were patterned in a resist film on Si substrate using deep ultraviolet lithography at 248 nm exposure wavelength. Details of the resist pattern fabrication process were described previously.[21] In the first step, a 65 nm thick Al_2O_3 layer was deposited by electron beam evaporation followed by a lift-off process. Subsequently, Cr (5 nm)/Py (25 nm) films were deposited on top of the patterned Al_2O_3 (65 nm) dots using electron beam evaporation at a rate of 0.2 Å s^{-1}. The Al_2O_3 layer was selectively removed using AZ 300 MIF standard developer in the final step. This step removed the Al_2O_3 layer with the Cr (5 nm)/Py (25 nm) above it, resulting in Py antidot

[a]*Department of Electrical and Computer Engineering, National University of Singapore, 117576, Singapore. E-mail: adekunle.o.adeyeye@durham.ac.uk*
[b]*Department of Physics, Durham University, South Rd, Durham, DH1 3LE, UK*

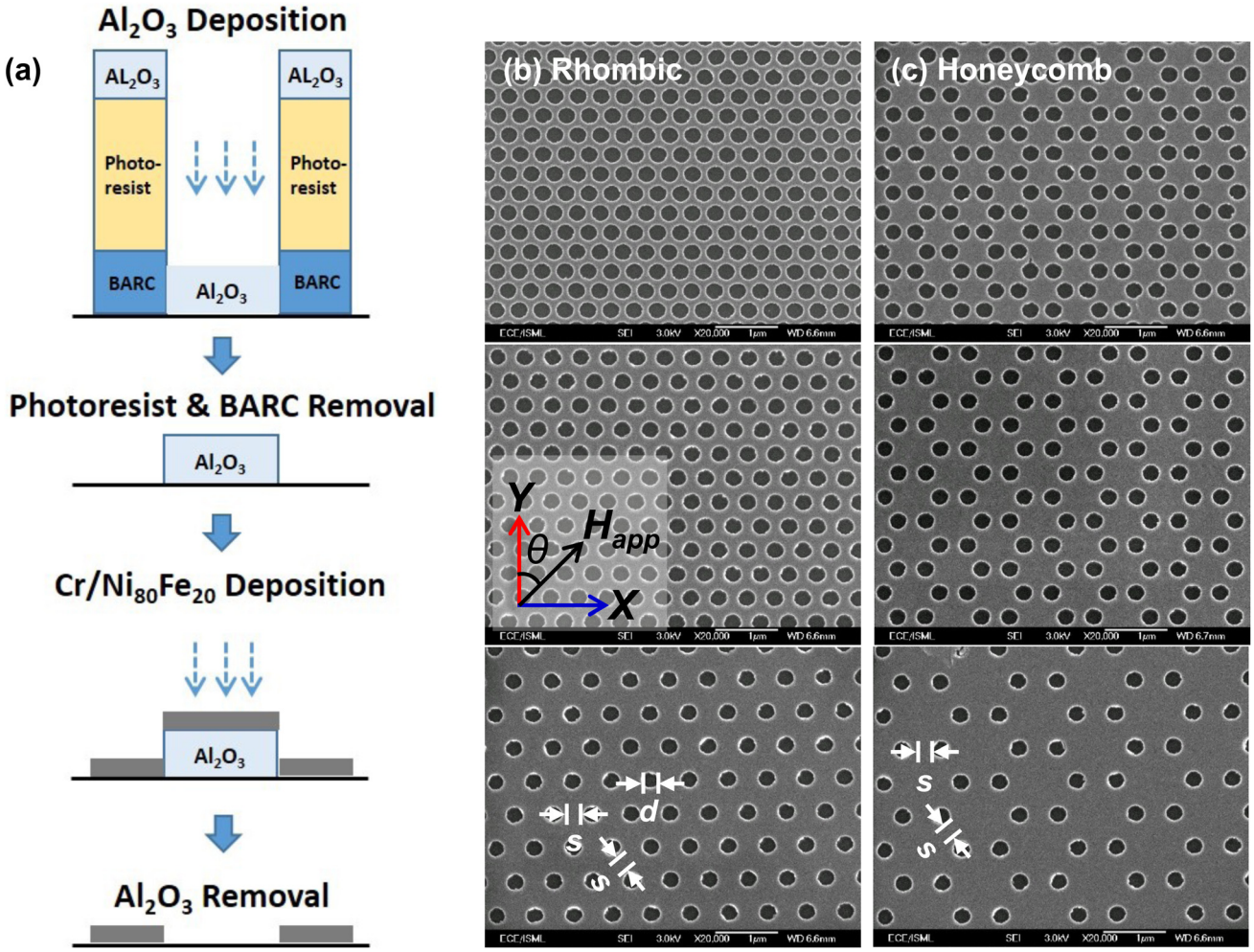

Fig. 1 (a) Schematic diagram of the fabrication process from resist hole patterns. (b) SEM images of 25 nm thick permalloy antidot structures of hole diameter d = 280 nm with inter-hole spacing s = 90, 170, and 345 nm for (a) rhombic, (b) square and (c) honeycomb lattices.

structures. Fig. 1(a) shows a schematic diagram of the fabrication processes from resist holes. Fig. 1(b and c) shows the scanning electron micrographs (SEM) of antidot structures (d = 280 nm) of the rhombic and honeycomb lattices. The spacing between the nearest neighbor holes along the X direction varies from 90 nm to 345 nm. The SEM images show highly ordered nanoscale antidot lattices with good uniformity. The direction of the external magnetic field H_{app} is denoted by an angle θ from the $+Y$ direction, as indicated as an insert in Fig. 1(b). To obtain the high-frequency response, an on-chip integrated coplanar waveguide (CPW) made up of Al_2O_3 (50 nm)/Cr (5 nm)/Pt (200 nm) was fabricated on top of the antidot structures using standard optical lithography and lift-off process. All the thin film depositions were done in a vacuum chamber with a base pressure of 4×10^{-8} Torr.

FMR measurements

The dynamic responses of the antidot structures were characterized using broadband ferromagnetic resonance spectroscopy with a vector network analyzer (VNA), which was connected *via* two G–S–G-type microwave probes to the on-chip CPW. The FMR measurements were performed at room temperature by sweeping the frequency from 100 MHz to 20 GHz for a given H_{app}. A reference background signal measured was subtracted from the FMR spectrum. In our investigation, we concentrated on the saturation region at H_{app} = −1400 Oe. This choice was motivated by the fact that magnetic states in this region are uniform and well-defined, enabling meaningful comparative studies of the antidot lattices (rhombic and honeycomb).

Simulations details

Micromagnetic simulations were performed using NIST's object-oriented micromagnetic framework (OOMMF) code.[22] The following standard material parameters were used for Py, namely: saturation magnetization $M_{S,Py}$ = 860 emu cm^{-3}, exchange constant $A_{Py} = 13 \times 10^{-7}$ erg cm^{-1}, and magnetocrystalline anisotropy $K_{1,Py}$ = 0 erg cm^{-3}. The magnetocrystalline anisotropies of the bulk Py film were assumed to be negligible compared to the shape anisotropy of the patterned structures.

A unit cell size of $5 \times 5 \times 5$ nm^3 was used in simulations. Time-dependent simulations were performed using a sinc wave excitation field $h_{sinc} = h_0 \frac{\sin(2\pi ft)}{t}$, where h_0 = 50 Oe, with a gyromagnetic ratio $\frac{\gamma}{2\pi} = 2.8\,\text{GHz kOe}^{-1}$ and a damping coefficient of α = 0.008. 2-D periodic boundary conditions were employed in these simulations to simulate the FMR response. The sinc wave was used in the simulation to yield a uniform excitation in the frequency domain. The dynamic simulation results were analyzed in the frequency domain after Fast Fourier Transform (FFT) processing.

Results and discussion

Rhombic antidot lattices

Fig. 2(a) shows the normalized experimental FMR absorption spectra of rhombic antidot lattices taken at H_{app} = −1400 Oe applied along the X and Y directions for d = 280 nm as a function of s. We observed that the FMR response is very sensitive to the inter-hole spacing s. A change in s results in a shift of mode frequency and a variation in mode number and intensity. For s = 90 nm, we observed two prominent modes (R1 at 9.5 GHz, R4 at 14.9 GHz) and two minor modes (R2 at 11.6 GHz, R3 at 12.8 GHz). The multiple resonance modes observed may be attributed to the inhomogeneous internal field distribution induced by the presence of holes.[16] For s = 170 nm, we observed five modes (R1, R2–5) and found the frequency of prominent mode R1 (f_{R1}) increases to 10.4 GHz. For s = 345 nm, only three main modes (R1′, R1 and R4) and a satellite mode at 11.7 GHz are observed, and f_{R1} is further increased to 11.2 GHz. The corresponding experimental FMR spectra of rhombic antidot lattices for the H_{app} applied along the Y direction as a function of s are significantly modified, as shown in Fig. 2(a). The significant difference in the FMR spectra between H_{app} along X and Y directions for the range of s investigated is attributed to the induced configurational anisotropy of the lattice symmetry.

We have performed a series of dynamic simulations to understand further the origin of the complex FMR spectra observed. Fig. 2(b) shows the corresponding simulated FMR spectra of rhombic antidot lattices as a function of s for H_{app} along the X direction. There is a good agreement between the experimental results (Fig. 2(a)) and simulated FMR spectra. We

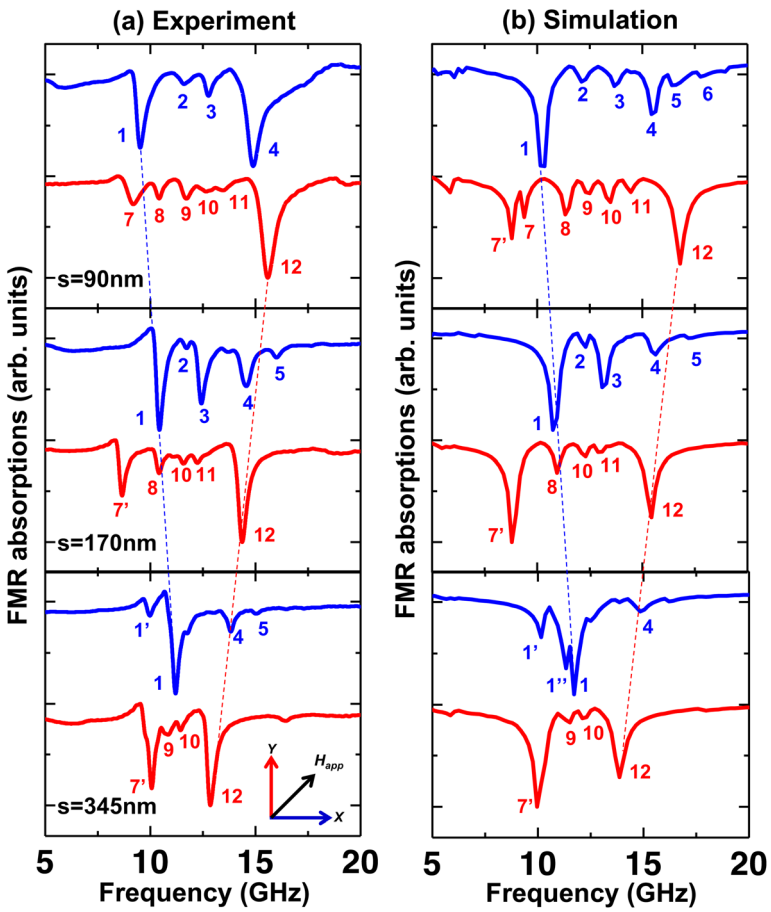

Fig. 2 (a) Experimental and (b) Simulated FMR spectra of 25 nm thick permalloy rhombic antidot lattices as a function of s taken at H_{app} = −1400 Oe along the X and Y directions.

have extracted the mode profile by performing FFT on in-plane magnetization components (m_Y) to identify the FMR modes. We have plotted the profiles for the observed modes for rhombic antidot lattices for H_{app} applied along the *X*-direction in Fig. 3(a) as a function of *s*. The simulated FMR spectrum of s = 90 nm identifies six distinct modes that reside along the *Y*-direction. We found that mode R1 is enclosed between two next-nearest neighbor holes in the same column, while modes R(2–6) are localized between the two nearest-neighbor holes. Mode R4 shows a stripe-like profile which connects two nearest-neighbor holes. Modes (R2, R3, R5, R6) show a blade-shaped profile with a strong spin precession amplitude at the edges of holes. Instead of three modes R(4–6) found in the simulation, we only observed one shoulder of mode R4 in the experiment, which may be attributed to the fact that modes (R5, R6) are too weak to be resolved in the experiment.

For s = 170 nm, mode R1 shows a profile similar to s = 90 nm but with a large amplitude near the hole edges. However, we observed that the R3 mode intensifies while the R2 mode weakens but persists in both the experimental and simulated data.

For s = 345 nm, however, fewer modes are observed. Instead of a single peak of mode R1 observed in the experiment, we found a dual peak with very close frequencies in the simulation. Mode R1 for s = 345 nm shows a very similar profile to that for s = 90 nm. We also noticed a satellite mode R1′, which resides along the *Y* direction, close to the hole edges. This may be attributed to the increasingly inhomogeneous magnetization near the edges of the holes when s/d is larger. It is possible to qualitatively understand the decrease in observed mode number as s is increased since the FMR responses of the antidot structures resemble that of the continuous un-pat-

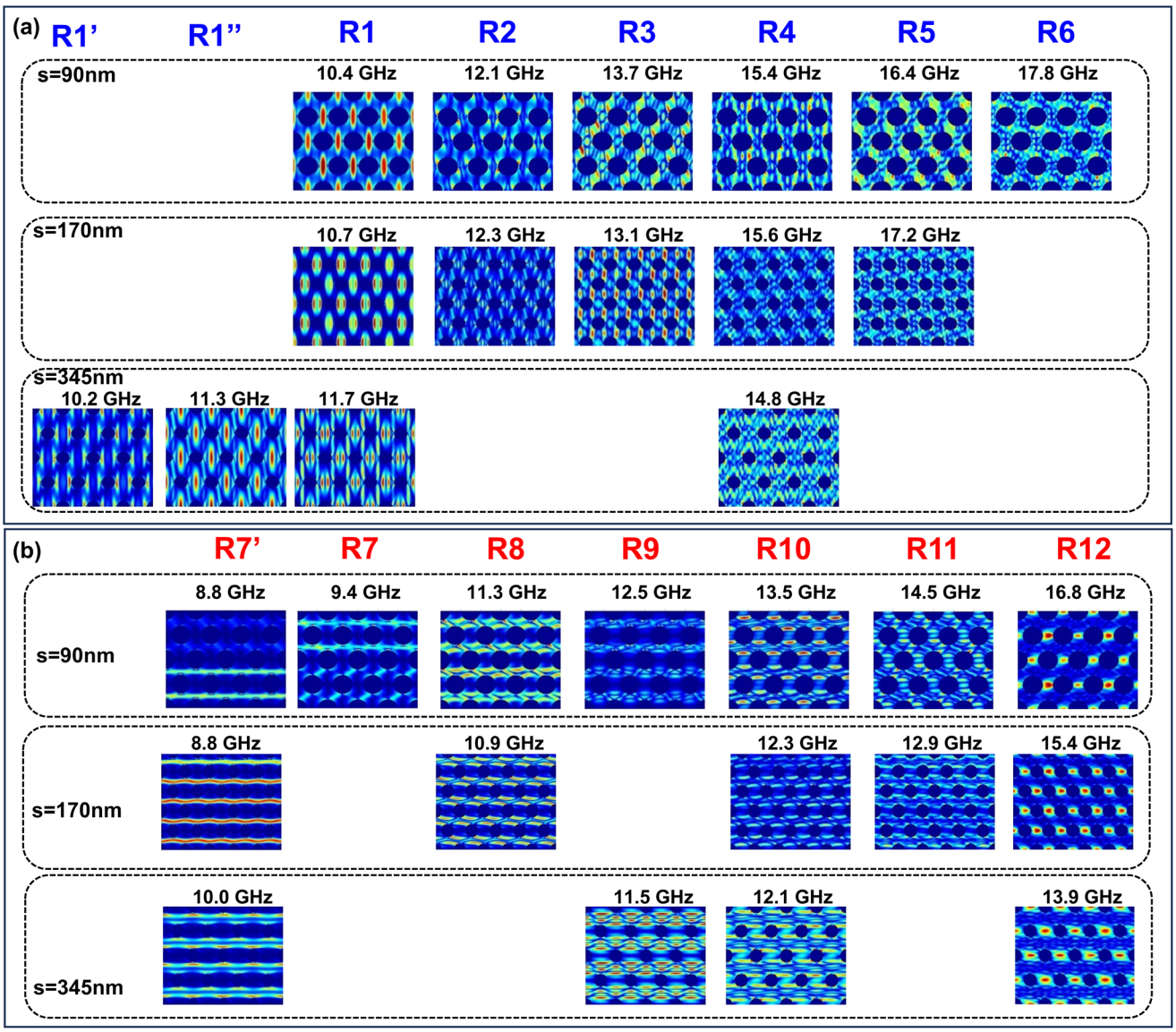

Fig. 3 Spatial profiles of modes in the simulated FMR spectra taken at H_{app} = −1400 Oe along (a) *X* and (b) *Y* directions of 25 nm thick permalloy rhombic antidot lattices as a function of *s*.

terned film, which has a single FMR mode with a resonance frequency f_{cont} = 11.2 GHz in our reference film. This is similar to the frequency of mode R1 at f_{cont} = 11.2 GHz for s = 345 nm.

The corresponding simulated FMR spectra of rhombic antidot lattices for the H_{app} applied along the Y direction as a function of s are shown in Fig. 2(b). The significant difference in the FMR spectra between H_{app} along X and Y directions for the range of s investigated is attributed to the induced configurational anisotropy of the lattice symmetry.

We have also extracted the profiles for the observed modes identified in Fig. 3(b) as a function of s. When H_{app} is applied along the Y direction, these observed modes reside along X. In the simulation, the excitation field hsinc, represented by a sinc wave, is applied perpendicular to the H_{app}. This configuration effectively stimulates the magnetization perpendicular to the hsinc direction, mimicking the actual experimental conditions.

For s = 90 nm, we found that mode R7 is localized in the area between rows of holes while mode R12 is localized between two nearest-neighbor holes of the same row. In the simulation, mode R7 is a dual peak with very close frequencies, labelled modes R7 and R7′. They display complementary spatial profiles due to a local variation in the dynamic magnetization, which is sensitive to the simulation. This dual peak manifests itself as a single peak in the experiment. Other minor modes R(8–11) show complicated spatial profiles, mainly located between rows of holes, because of hybridization effects with the higher frequency mode.[16]

For s = 170 nm, we found that the intensity of mode R7 becomes more pronounced than s = 90 nm, which was also confirmed in the experiment. We did not observe mode R9, probably because it is too weak to be identified. For s = 345 nm, the intensity of mode R7 is further increased, and it is confirmed in the simulation. The profile of mode R7 for s = 345 nm shows a symmetry node in the middle region between rows of holes with a peak amplitude near the holes' edges. This is quite different when compared with the profile of mode R7 for s = 90 and 170 nm. The increase in the intensity of mode R7 as s is increased can be explained by considering its resonance area, which is extended in the area between rows of holes. When s is increased, the contribution from this area is increased due to more materials (increasing the width of the resonant area), so mode R7 becomes more pronounced. Interestingly, fewer modes are identified for s = 345 nm, probably because different modes combined or are too weak to be observed.

For H_{app} along the X and Y directions, we will discuss the frequency shift of the most prominent modes, *i.e.*, R1 and R12. In the experimental spectra, we observed the frequency of mode R1 (f_{R1}) increases while mode R12 (f_{R12}) decreases when s is increased from 90 nm to 345 nm in agreement with the simulated FMR spectra. The frequency shift can be explained by considering the variation of the demagnetizing field with the increase of s for the resonance areas of modes R1 and R12. The X and Y components of the demagnetizing field (H_d) for H_{app} along the X and Y directions at point c have been extracted from OOMMF simulations as functions of s and plotted in Fig. 4. We observed that the H_d at point c becomes negative when H_{app} is applied along the +X direction and positive when H_{app} is applied along the +Y direction. From a qualitative standpoint, this behavior can be elucidated by treating the region around point c as a rectangular magnet outlined by the green dashed line. Point c experiences a greater demagnetizing field (opposite to the magnetization orientation) when H_{app} is along the +X direction than when H_{app} is along the +Y direction. This discrepancy arises because the X direction represents the short axis of the rectangular magnet, leading to a negative H_d at point c when H_{app} is along the +X direction. It is important to note that the actual value of H_d is influenced not only by the green magnet but also by the collective field exerted by the five magnets (one green and four yellow magnets). When H_{app} is applied along the +Y direction, H_d becomes positive, considering the contribution from the four yellow magnets. The absolute values of H_d exhibit a decreasing trend due to the increasing spacing between magnets. As the spacing (s) increases, the fields exerted by these five magnets diminish. Consequently, the nanostructure behaves more akin to a large film with increasing s, causing H_d-x and H_d-y to converge to 0.

As a result, point c has a larger internal field (H_{int}) for H_{app} applied along Y ($H_{int} = H_{app} + H_d$) than H_{app} along X ($H_{int} = H_{app} - H_d$). This explains the larger resonance frequency of mode R12 compared to mode R1 for all the s investigated. We also observed that the absolute value of H_d decreases with an increase in s for both H_{app} directions. Consequently, for mode R1, the H_{int} of its resonance area increases as s increases, while for mode R12, the H_{int} decreases as s increases. It explains how f_{R1} increases while f_{R12} decreases with an increase in s.

We can also understand the change of f_{R1} and f_{R12} with s qualitatively. As s increases, the antidot structure will behave more like a continuous un-patterned film with a resonance frequency (f_{cont} = 11.2 GHz in our reference film) independent of H_{app} directions. So f_{R1} and f_{R12} approach the f_{cont} of the con-

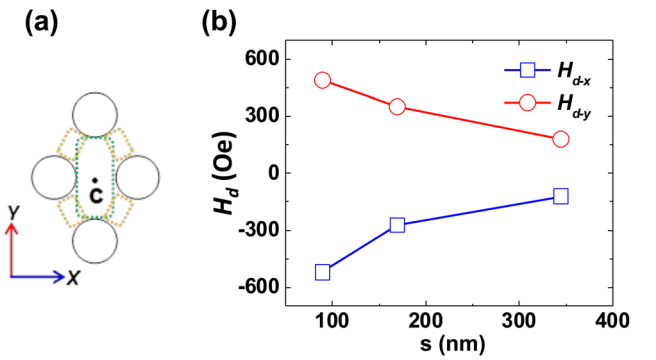

Fig. 4 (a) Schematic diagram of the rhombic unit cell. Point c is the center of the rhombic unit cell. (b) The X and Y components of the demagnetizing field (H_d) for H_{app} along the X and Y directions respectively, at point c as a function of s.

tinuous film when s is increased. This may, therefore, explain the convergent trend of f_{R1} and f_{R12} as s is increased.

Fig. 5(a) shows the experimental FMR absorption spectra of honeycomb antidot lattices taken at $H_{app} = -1400$ Oe along the X and Y directions as a function of s. Unlike rhombic lattices, the FMR spectra for H_{app} along X and Y directions are similar. The corresponding simulated FMR spectra of honeycomb antidot lattices for H_{app} along the X and Y directions as a function of s are shown in Fig. 5(b). There is good agreement between the experimental and simulated results.

For s = 90 nm, three distinct modes H1 (9.1 GHz), H2 (12.1 GHz) and H3 (15.8 GHz) is observed for the spectrum of H_{app} along X direction and three modes H4 (9.9 GHz), H5 (12 GHz) and H6 (16.5 GHz) for H_{app} along Y direction. As s is increased to 170 nm, we observed that the prominent mode H2 splits and the frequency of prominent mode H5 (f_{H5}) decreases to 11.8 GHz. As s is further increased to 345 nm, mode H2 (f_{H2}) frequency decreases to 11.6 GHz, and mode H5 (f_{H5}) decreases to 11.5 GHz. We have observed an overall convergence of modes H (1–3) and H(4–6) as s increases.

We have plotted the profiles for the observed modes H (1–6) for different s in Fig. 6. For s = 90 nm, we found that mode H1 extends as a continuous resonant stripe along Y while mode H4 extends as another continuous stripe along X enclosed by the holes. Note that there is only a single stripe for mode H1 within one honeycomb unit cell, while there are two stripes for mode H4. Modes H2 and H5 are localized at the central region of the honeycomb unit cell. Mode H3 is enclosed between two nearest-neighbor holes in the rows of holes along $\theta = -\frac{\pi}{6}$ directions, and H6 is enclosed between two nearest-neighbor holes in the horizontal rows of holes. For s = 170 nm, modes H1, H4, H5 and H6 show a similar profile to that for s = 90 nm. Mode H2 becomes triplet modes and is localized in different areas within the hexagonal unit cell. Mode H3 is enclosed between two nearest-neighbor holes in the rows of holes along $\theta = \frac{\pi}{6}$ directions. For s = 345 nm, mode H1 extends as a more uniform resonant stripe along Y compared with the cases of s = 90 and 170 nm, which show a more concentrated spin precession amplitude between two horizontal nearest-neighbor holes. Mode H3 becomes too weak to be identified, while Mode H4 displays a symmetry node in the middle region between rows of holes with a peak amplitude near the holes' edges. This mode profile evolution of H4 is similar to that of mode R7 in the rhombic antidot lattice.

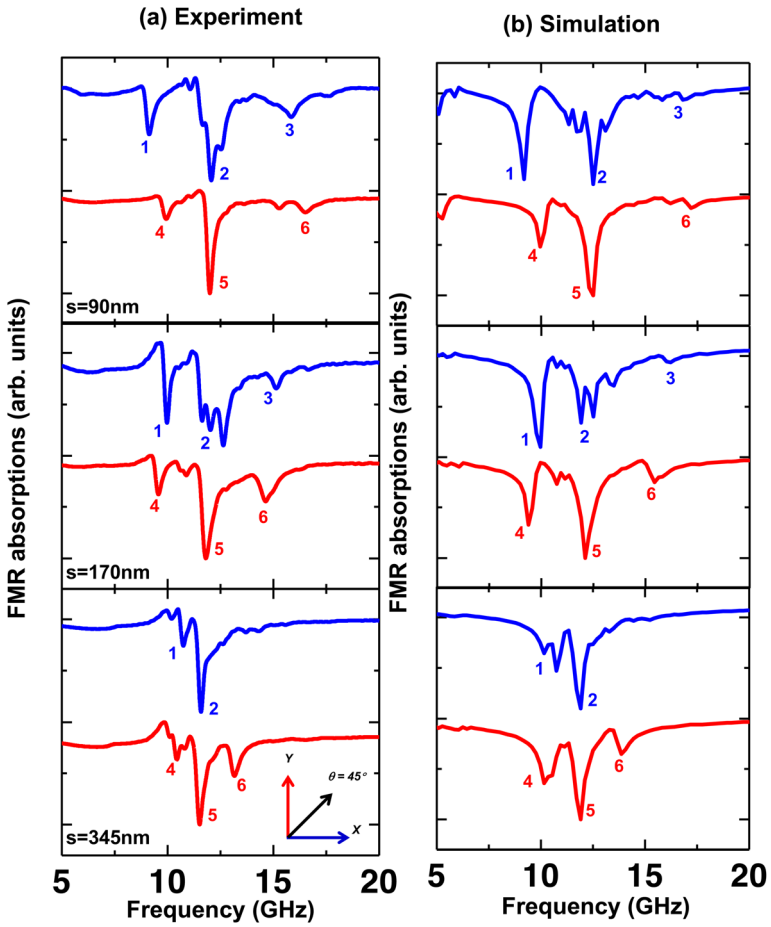

Fig. 5 (a) Experimental and (b) Simulated FMR spectra of 25 nm thick permalloy honeycomb antidot lattices as a function of s taken at H_{app} = −1400 Oe along the X and Y directions.

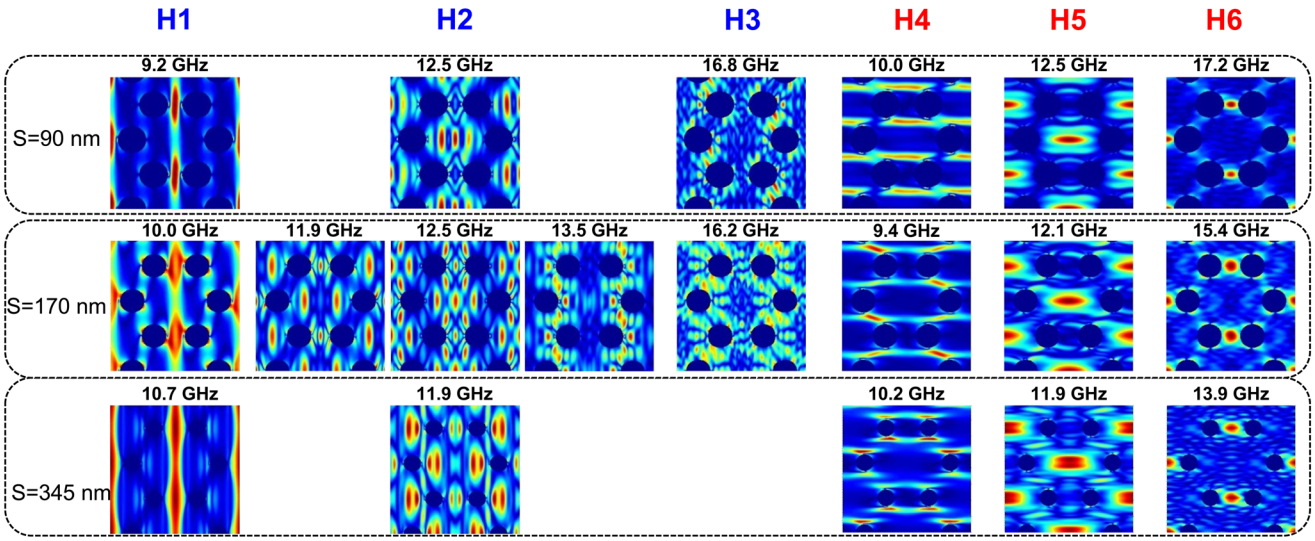

Fig. 6 Spatial profiles of modes in the simulated FMR spectra taken at H_{app} = −1400 Oe along *X* and *Y* directions of 25 nm thick permalloy honeycomb antidot lattices as a function of *s*.

It is worth noting that the resonance frequency variations with H_{app} direction and *s* are less pronounced in the honeycomb antidot lattice than in the rhombic antidot lattice discussed earlier. For example, as *s* is increased from 90 nm to 345 nm, the frequency shifts of prominent modes H2 and H5 are small (~0.5 GHz) compared with what was observed for rhombic antidot lattice where a distinct frequency shift of 1.7 GHz for mode R1 and 2.7 GHz for mode R12 with *s* increasing from 90 nm to 345 nm. The marked difference between rhombic and honeycomb antidot lattices is attributed to an additional hole at the central region of the hexagonal unit cell in the rhombic lattice. The presence of an additional hole induces a larger variation in demagnetisation field as a function of *s*. Consequently, it produces a larger resonance frequency modification with *s* and different H_{app} directions.

Conclusions

In summary, we have systematically investigated the effects of inter-hole spacing and lattice (rhombic and honeycomb) arrangements on the dynamic responses of $Ni_{80}Fe_{20}$ antidot structures. We also showed that the dynamic behaviors of antidot structures are very sensitive to the *s* and H_{app} directions. By changing the *s* and H_{app} direction, a marked variation in mode frequency, mode intensity and number of modes is observed. Our experimental results are in good agreement with micromagnetic simulations. These results may find useful applications in the design of tunable microwave filters and magnonic devices.

Author contributions

A. O. A. conceived the project. CT fabricated the samples and carried out the experiments. A. O. A. supervised the overall project. All authors discussed the results and co-wrote the manuscript.

Conflicts of interest

There are no conflicts to declare.

Acknowledgements

A.O.A would like to acknowledge the funding from the Wolfson Foundation and Royal Society. The authors thank Dr Navab Singh for the DUV templates.

References

1 A. V. Chumak, A. A. Serga and B. Hillebrands, *J. Phys. D: Appl. Phys.*, 2017, **50**, 244001.
2 Z. K. Wang, V. L. Zhang, H. S. Lim, S. C. Ng, M. H. Kuok, S. Jain and A. O. Adeyeye, *Appl. Phys. Lett.*, 2009, **94**, 083112.
3 A. Barman, G. Gubbiotti, S. Ladak, A. O. Adeyeye, M. Krawczyk, J. Grafe, C. Adelmann, S. Cotofana, A. Naeemi, V. I. Vasyuchka, B. Hillebrands, S. A. Nikitov, H. Yu, D. Grundler, A. V. Sadovnikov, A. A. Grachev, S. E. Sheshukova, J. Y. Duquesne, M. Marangolo, G. Csaba, W. Porod, V. E. Demidov, S. Urazhdin, S. O. Demokritov, E. Albisetti, D. Petti, R. Bertacco, H. Schultheiss, V. V. Kruglyak, V. D. Poimanov, S. Sahoo, J. Sinha, H. Yang, M. Munzenburg, T. Moriyama, S. Mizukami, P. Landeros, R. A. Gallardo, G. Carlotti, J. V. Kim, R. L. Stamps, R. E. Camley, B. Rana, Y. Otani, W. Yu, T. Yu, G. E. W. Bauer, C. Back, G. S. Uhrig, O. V. Dobrovolskiy,

B. Budinska, H. Qin, S. van Dijken, A. V. Chumak, A. Khitun, D. E. Nikonov, I. A. Young, B. W. Zingsem and M. Winklhofer, *J. Phys.: Condens.Matter*, 2021, **33**, 413001.

4 Z. K. Wang, V. L. Zhang, H. S. Lim, S. C. Ng, M. H. Kuok, S. Jain and A. O. Adeyeye, *ACS Nano*, 2010, **4**, 643–648.

5 S. Neusser and D. Grundler, *Adv. Mater.*, 2009, **21**, 2927–2932.

6 S. Tacchi, F. Montoncello, M. Madami, G. Gubbiotti, G. Carlotti, L. Giovannini, R. Zivieri, F. Nizzoli, S. Jain, A. O. Adeyeye and N. Singh, *Phys. Rev. Lett.*, 2011, **107**, 127204.

7 R. Mandal, S. Saha, D. Kumar, S. Barman, S. Pal, K. Das, A. K. Raychaudhuri, Y. Fukuma, Y. Otani and A. Barman, *ACS Nano*, 2012, **6**, 3397–3403.

8 D. Kumar, P. Sabareesan, W. Wang, H. Fangohr and A. Barman, *J. Appl. Phys.*, 2013, **114**, 023910.

9 J. Ding, D. Tripathy and A. O. Adeyeye, *Europhys. Lett.*, 2012, **98**, 16004.

10 J. Ding, D. Tripathy and A. O. Adeyeye, *J. Appl. Phys.*, 2011, **109**, 07D304.

11 S. Neusser, G. Duerr, H. G. Bauer, S. Tacchi, M. Madami, G. Woltersdorf, G. Gubbiotti, C. H. Back and D. Grundler, *Phys. Rev. Lett.*, 2010, **105**, 067208.

12 S. Tacchi, B. Botters, M. Madami, J. W. Kłos, M. L. Sokolovskyy, M. Krawczyk, G. Gubbiotti, G. Carlotti, A. O. Adeyeye, S. Neusser and D. Grundler, *Phys. Rev. B: Condens. Matter Mater. Phys.*, 2012, **86**, 014417.

13 R. Bali, M. Kostylev, D. Tripathy, A. O. Adeyeye and S. Samarin, *Phys. Rev. B: Condens. Matter Mater. Phys.*, 2012, **85**, 104414.

14 T. Schwarze, R. Huber, G. Duerr and D. Grundler, *Phys. Rev. B: Condens. Matter Mater. Phys.*, 2012, **85**, 134448.

15 O. N. Martyanov, V. F. Yudanov, R. N. Lee, S. A. Nepijko, H. J. Elmers, R. Hertel, C. M. Schneider and G. Schönhense, *Phys. Rev. B: Condens. Matter Mater. Phys.*, 2007, **75**, 174429.

16 S. Tacchi, M. Madami, G. Gubbiotti, G. Carlotti, A. O. Adeyeye, S. Neusser, B. Botters and D. Grundler, *IEEE Trans. Magn.*, 2010, **46**, 1440–1443.

17 S. Neusser, B. Botters, M. Becherer, D. Schmitt-Landsiedel and D. Grundler, *Appl. Phys. Lett.*, 2008, **93**, 122501.

18 S. Neusser, G. Duerr, S. Tacchi, M. Madami, M. L. Sokolovskyy, G. Gubbiotti, M. Krawczyk and D. Grundler, *Phys. Rev. B: Condens. Matter Mater. Phys.*, 2011, **84**, 094454.

19 S. Tacchi, P. Gruszecki, M. Madami, G. Carlotti, J. W. Klos, M. Krawczyk, A. Adeyeye and G. Gubbiotti, *Sci. Rep.*, 2015, **5**, 10367.

20 J. Sklenar, V. S. Bhat, L. E. DeLong, O. Heinonen and J. B. Ketterson, *Appl. Phys. Lett.*, 2013, **102**, 152412.

21 A. O. Adeyeye and N. Singh, *J. Phys. D: Appl. Phys.*, 2008, **41**, 153001.

22 M. J. Donahue and D. G. Porter, *Interagency Report NISTIR 6376*, National Institute of Standards and Technology, Gaithersburg, MD, 1999.